HOSTED BY
ELSEVIER
Available online at www.sciencedirect.com
ScienceDirect
Soils and Foundations 57 (2017) 439–452
SOILS AND FOUNDATIONS
www.elsevier.com/locate/sandf

Sub-particle-scale investigation of seepage in sands

Howard F. Taylor [a,*], Catherine O'Sullivan [a], Way Way Sim [b,1], Simon J. Carr [c]

[a] Dept. of Civil & Environmental Eng., Imperial College London, UK
[b] Atkins, Bristol, UK
[c] Centre for Micromorphology, School of Geography, Queen Mary University of London, UK

Received 10 June 2016; received in revised form 16 January 2017; accepted 21 February 2017
Available online 22 May 2017

Abstract

While seepage poses significant challenges to many geotechnical projects and hydraulic conductivity is a key soil property, the fundamental pore-scale understanding of the water flow in soil is poor. The seepage velocities considered in geotechnical engineering are area-averaged flow rates and their relation to the actual fluid velocity is unclear. Some of the predictive formulae for sand currently used in engineering practice were developed using simplified particle-scale analytical models whose validity is not well-established. Recent advances in modelling and imaging enable these uncertainties associated with seepage to be addressed and this paper proposes a first principles simulation approach in which the flow in the void space is modelled by applying Computational Fluid Dynamics (CFD) to void geometries obtained using X-ray micro-Computed Tomography (microCT). The model was verified by comparing it to hydraulic conductivity data from laboratory permeameter tests on the same materials. The generated data provide significant sub-particle-scale insight into fluid velocities and head loss. The results are used to show that the existing models for predicting hydraulic conductivity struggle to account for the full range of particle variables and fail to explain the true governing variables, which relate to the micro-scale properties of the void space.

Keywords: Seepage; Sands; Permeability; Numerical modelling; Laboratory tests (**IGC**: D04/E13)

1. Introduction

In seepage analyses, geotechnical engineers typically consider soil as a porous continuum and apply Darcy's law, assigning a hydraulic conductivity or permeability (k) to the soil continuum. The importance of understanding the fundamental seepage process is emphasized in textbooks including those by Harr (1990) and Mitchell and Soga (2005). The present contribution improves upon the schematic diagrams and analytical models proposed in these texts by using high resolution 3D images and computational fluid dynamics (CFD), with a discretization resolution that is smaller than the particle size, to quantify the fluid flow within the void space of sands. The insight that can be obtained from this approach can advance the understanding of internal instability and filtration (Dallo and Wang, 2016; Kenney et al., 1985; Kézdi, 1979); ground improvement (Kim and Whittle, 2009); the mechanical dispersion of contaminants (discussed in Fetter (1994) and Fitts (2012)); and well development in in-situ permeability testing (Cashman and Preene, 2001), etc.

Previous studies have combined microCT imaging and network models to study porous sandstone (Mostaghimi et al., 2013; Pereira Nunes et al., 2015; Piller et al., 2014), and network models have been proposed for granular materials (e.g., Chareyre et al., 2012). However, the more

Peer review under responsibility of The Japanese Geotechnical Society.
* Corresponding author at: Dept. of Civil & Environmental Eng., Imperial College London, SW7 2AZ, UK.
E-mail address: howardftaylor@hotmail.co.uk (H.F. Taylor).
[1] Formerly Imperial College London, UK.

http://dx.doi.org/10.1016/j.sandf.2017.05.010
0038-0806/

open void geometry in sands makes these models difficult to apply (Taylor et al., 2016). Numerical models (Yazdchi and Luding, 2013) and empirical studies (Indraratna et al., 2012) support the hypothesis that the seepage behaviour in granular materials is governed by the narrowest points in the void space, referred to as 'constrictions'.

This paper describes the experimental procedure to acquire microCT images; pore-scale CFD simulations; and model verification by a comparison with laboratory permeameter tests. The generated data enable an analysis of the local velocities and the fundamental mechanisms of head loss in sand. The technique is applied to reassess the basis for the Kozeny-Carmen equation and other equations used to predict hydraulic conductivity in geotechnical analyses.

2. Acquisition of void topography

2.1. Specimen preparation

Referring to Table 1 and Fig. 1, four materials were chosen to enable consideration of the influence of particle size distribution (PSD) and particle shape. Each material sample was prepared in a triaxial cell using the dry deposition method (Ishihara, 1993) and densified to a relative density of approximately 50–70% (based on the maximum and minimum void ratios achievable by this deposition method) by tapping the base of the cell. Air suction of approximately 30 kPa was applied to the top cap temporarily, to maintain sample integrity until the cell was assembled, and then cell air pressure of 30 kPa was applied. To preserve the void structure and to produce samples small enough to allow high resolution imaging (Cnudde and Boone, 2013), triaxial samples were impregnated with resin and sub-sampled, as described in Fonseca et al. (2013). Referring to Fig. 2 (a), the resin was drawn up from the base by elevating the resin container and applying a small amount of air suction (≈1 kPa) at the top cap. The resin was allowed to cure for at least 24 h before coring 9 mm central sub-samples. For test repeatability, two separate triaxial samples were prepared for material Sand-Cu3, identified as [1] and [2], making a total of five samples.

2.2. MicroCT imaging

The 9-mm cores were scanned using a Nikon XT–H–225 microCT scanner at Queen Mary University of London, using the scanning parameters given in Table 2. Image processing involved median filtering and threshold segmentation, using the method proposed by Otsu (1979), to produce the 3D binary images shown in Fig. 3 where each voxel is designated to be solid (grey in Fig. 3) or void (transparent) depending on the level of X-ray attenuation.

The samples were inhomogeneous, and thus, the PSDs (as presented in Fig. 1) were determined for each core using the microCT data, following the approach detailed in Fonseca et al. (2012). Watershed segmentation of the particle phase was used to identify individual particles; employing a principle component analysis, the particle orientations were determined and used to define an orthogonal bounding box around each particle. The intermediate length of the bounding box was taken as the particle size for use in the PSD. For comparison, the points in Fig. 1, denoted as "*LAB* D_{10} & D_{60}", indicate the particle sizes for 10% passing and 60% passing by mass, respectively, measured in the laboratory by dry sieving. These points show a good agreement between the image-based particle sizes and conventional laboratory methods. The materials were characterised by their coefficient of uniformity, $C_u = D_{60}/D_{10}$ (with values of either 1.5 or 3), and their material type ('Sand' denotes Leighton Buzzard Sand, while 'Beads' denoted aluminium borosilicate glass beads).

Any approach to partitioning the continuous void space will be subjective. In the current study, the constrictions were geometrically identified following the approach described in Taylor et al. (2015). Referring to Fig. 4, the void space was segmented into discrete void regions using watershed segmentation. This process defines the void boundaries; constriction diameters were then calculated as the local maxima of the distance map on the boundary surface, as this defines the largest spheres which can fit across the boundary. A post-processing step is required to remove the extraneous local maxima so that only meaningful constrictions are identified (full details are given in Taylor et al. (2015)). Taylor et al. (2015) demonstrated that this approach gives results that are comparable with other geometric partitioning algorithms (notably the Delaunay triangulation method used in DEM studies (Reboul

Table 1
Material properties.

Name	Material	Target D_{10} (mm)	Target D_{60} (mm)	Median sphericity[a]	Median aspect ratio[a]	Median convexity[a]
Sand-Cu3[1]	Leighton Buzzard Sand	0.4	1.2	0.9	0.75	0.95
Sand-Cu3[2]		0.4	1.2			
Sand-Cu1.5		0.5	0.75			
Beads-Cu3	Borosilicate Glass Beads	0.4	1.2	0.95	0.97	0.97
Beads-Cu1.5		0.5	0.75			

[a] Measured by laser scanning as described in Cavarretta et al. (2012) and Altuhafi et al. (2013).

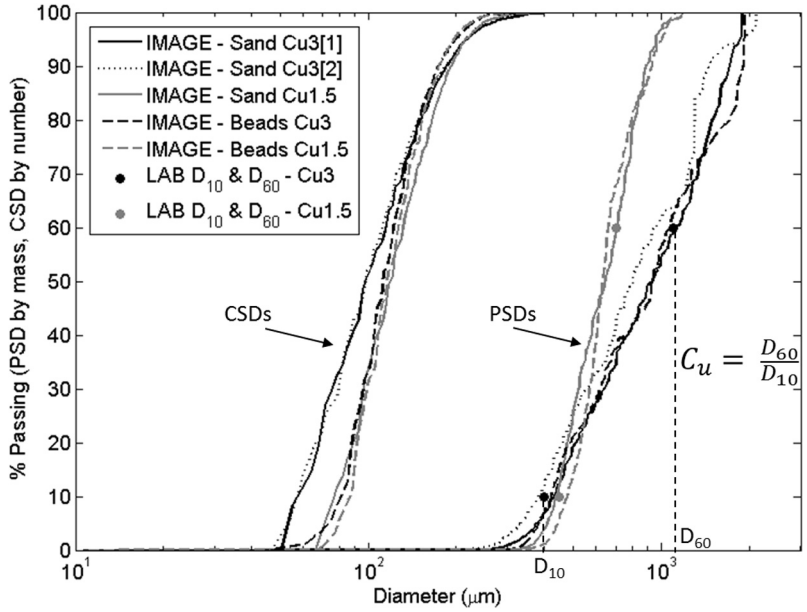

Fig. 1. Particle and constriction size distributions for all materials analyzed. D_{10} and D_{60} values measured in the lab, using dry sieving, are also shown as dots (*LAB* D_{10} & D_{60}).

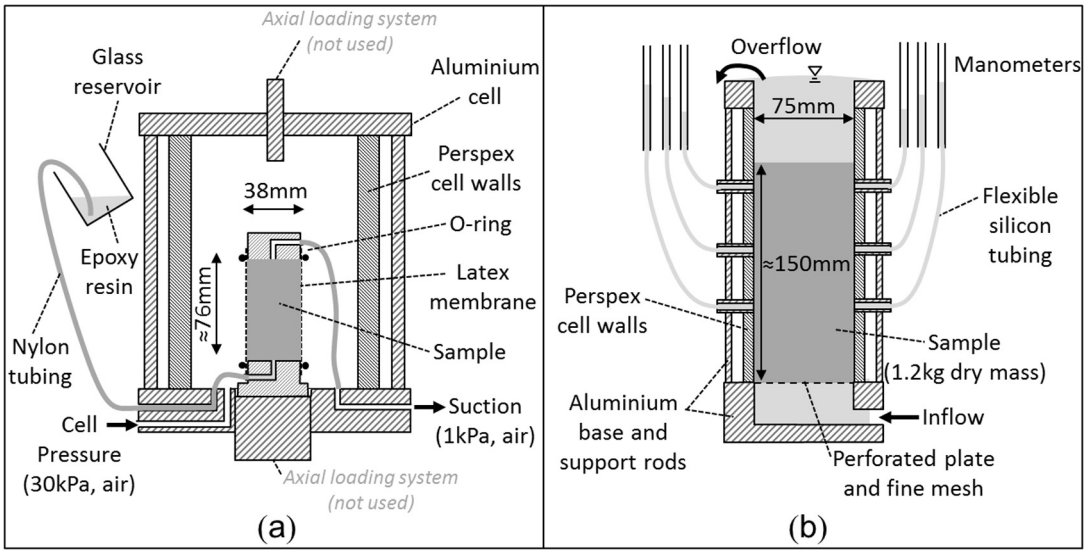

Fig. 2. Schematics of laboratory apparatus: (a) resin impregnation set-up and (b) permeameter.

Table 2
MicroCT scanning parameters.

Name	Filter	Voltage (kV)	Current (μA)	Exposure time (ms)	Voxel size (micron)	Particle diameters (voxels)
Sand-Cu3[1]	1 mm Copper	265	150	1415	11.3	25–180
Sand-Cu3[2]					9.8	30–205
Sand-Cu1.5					11.3	35–90
Beads-Cu3					10.3	30–200
Beads-Cu1.5					10.7	40–95

et al., 2010; Shire and O'Sullivan, 2016), as well as image-based methods such as the medial axis (Homberg et al., 2014; Lindquist et al., 2000) and maximal ball method (Dong and Blunt, 2009)). However, the watershed method has the advantages of greater adaptability for different materials and improved 3D visualization of constrictions. The size of voids and void constrictions (and hence, the analyses discussed in this paper) are sensitive to the image

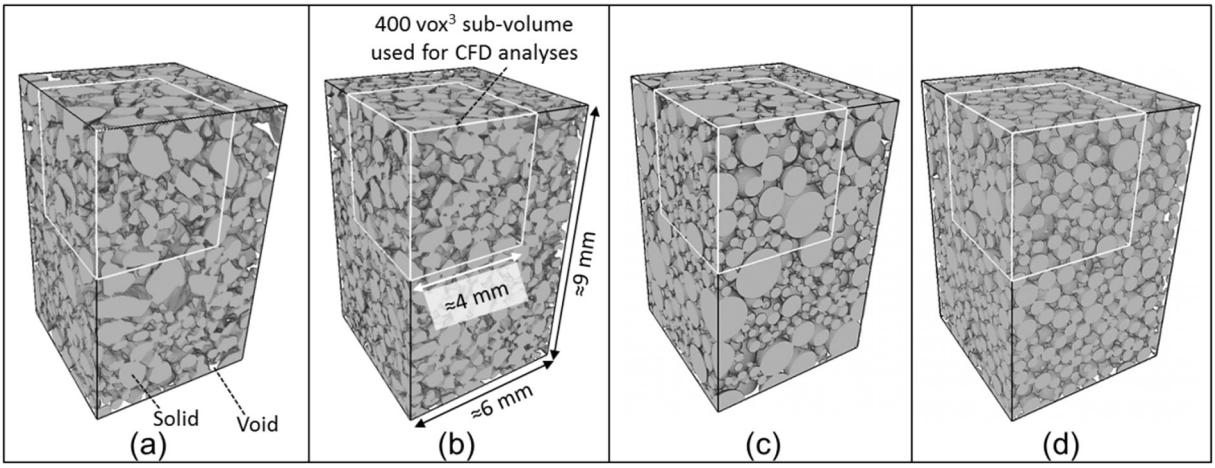

Fig. 3. 3D images of materials analyzed: (a) Sand-Cu3[1], (b) Sand-Cu1.5, (c) Beads-Cu3, and (d) Beads-Cu1.5.

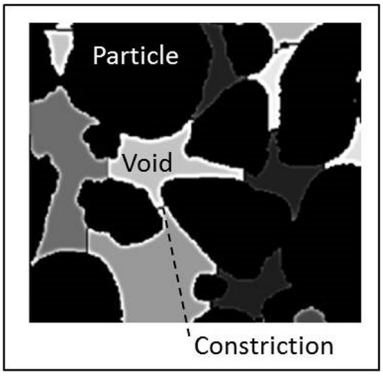

Fig. 4. Watershed segmentation method to measure geometric constrictions.

processing methodology. Image processing parameters were selected based on the recommendations by Taylor et al. (2015) and were kept consistent for the five samples analyzed in this study so that valid conclusions could be drawn as to how the void space and the sub-particle flow regimes differed for these five samples.

Constriction size measurements for the five specimens are presented in Fig. 1 as constriction size distributions (CSDs). The CSD curves demonstrate the effects of C_u and particle shape on constriction sizes, where a higher C_u results in a wider range of constriction sizes; and angular particles produce more constrictions at both the upper and lower ends of the constriction size range, compared to spherical particles.

3. Computational Fluid Dynamics (CFD) simulations

3.1. Model development

CFD simulations were performed using the open source CFD solver OpenFOAM (Version 2.4.0, 2015) which has been used successfully in similar studies on porous rocks (Mostaghimi et al., 2013; Pereira Nunes et al., 2015; Piller et al., 2014; Raeini et al., 2012). OpenFOAM solves the conservation of mass and momentum equations iteratively over a finite volume mesh, using the Semi-Implicit Method of Pressure Linked Equations, or SIMPLE algorithm (OpenFOAM Foundation, 2014; Raeini et al., 2012). The cell size used in the CFD simulations was one voxel, which was significantly smaller than the particle size. A 'no slip' boundary condition was applied at the particle surfaces, meaning that there was no flow across these boundaries and that the velocities along the boundary were zero. In contrast to coupled DEM studies using either CFD (e.g., Zeghal and El Shamy, 2004) or the lattice Boltzman technique (e.g., Galindo-Torres, 2013) to resolve the fluid flow, these simulations are not coupled, i.e., the transfer of momentum between particles and fluid is not considered and the particles are assumed to remain static under the fluid flow. Once the iterative solution has converged, the outputs are pressure and velocity values at the center of each mesh cell.

Finite volume meshes were generated by converting the voxelized binary images, shown in Fig. 3, into 3D stereolithographic surfaces (.stl format) using the open source imaging software ImageJ (Rasband, 2012), and then filling the void within this surface with a polyhedral mesh using the open source graphical user interface HELYX-OS (Engys, 2015). Sub-volumes, $400 \times 400 \times 400$ voxels in size, were analyzed, rather than the full images, so that mesh generation and the convergence of the CFD solver could each be achieved within 24 h on a desktop computer with 144 GB of RAM. The length of these sub-volumes was relatively small, approximately 5–7 times D_{50} (median particle diameter); and thus, to assess whether the sub-volumes were representative elementary volumes (REVs), void ratio variations were measured in cubic sub-volumes with varying sizes and at varying locations within the images. The variation in void ratio decreased as the sub-volume size increased from 100^3 to 400^3 voxels, but no significant improvement was achieved by a further increase to 500^3 voxels, supporting the use of 400^3 voxel sub-volumes

as REVs. For four of the five sub-volumes, the void ratios were within ±0.01 (≈ ± 2%) of the average for the full image, while the difference was +0.03 (≈ + 6%) for Sand-Cu3[1]. This difference in void ratio indicates that the Sand-Cu3[1] sub-sample may not be representative of the average properties for larger samples; consequently, the hydraulic conductivity of this sub-sample is expected to be higher than that of larger samples. Mostaghimi et al. (2013) found the REV for hydraulic conductivity measurements to be larger than that required to capture the void ratio; hence, a comparison with laboratory permeameter measurements (discussed below) was used to demonstrate whether or not the smaller sub-volumes were representative.

Before analyzing the microCT images, the OpenFOAM solver was validated using a synthesized 3D image of a periodically constricted tube (Fig. 5(a)), with a voxel size comparable to the microCT images. The velocity outputs from the CFD solution were interpolated to give values at the center of each voxel, producing the normalized values shown in Fig. 5(b). The velocity values were typically within ±2% of the analytical solution given by Sisavath et al. (2001) which was deemed acceptable. However, values within 5 voxels of the inlet and outlet boundaries had errors up to ±10% from the analytical solution. Fig. 5(c) shows pressure values along the tube centerline and supports the earlier hypothesis that the pressure loss is governed by the constrictions.

Rajon et al. (2002) showed that voxelization can overestimate the surface area by up to 50% for 3D spheres. To minimize this error, which will impact the CFD simulations, the void geometry was smoothed using the 'smooth' function in Rhino 5.0 (Robert McNeel & Associates, 2015), as shown for a single particle in Fig. 6. Test images of voxelized spheres (Fig. 6(c)) showed that the smoothing process reduced the error in surface area from 10–20% down to <5%. To determine the sensitivity of the OpenFOAM results to smoothing, simulations were performed for 'spheres' (actually polyhedral, as shown in Fig. 7(a)) generated in the HelyxOS graphical user interface and also for voxelized spheres with the same centers and radii, before and after smoothing (Fig. 7(c) and (d), respectively). Relative to the polyhedral 'spheres', the mean velocity in the flow direction was 7% lower for the voxelized spheres and this error was reduced by smoothing to 4%. The validation case for a periodically constricted tube, shown in Fig. 5, was also re-run with a smoothed surface, reducing the mean error from ±2% down to ±1%.

3.2. Sub-grain scale model of seepage

Fig. 8 shows the Beads-Cu3 sub-volume, including the boundary conditions applied in the CFD simulation. The pressure gradient of 0.001 kPa across the sub-volume is equivalent to a hydraulic gradient of 0.025; as the resultant Reynolds number ≪1 the flow is laminar. As in the validation case, the velocity data obtained within about 5 voxels of the input and output boundaries contained some anomalous values. As a result, the data within 10 voxels of each boundary were ignored in all subsequent analyses. The 'symmetry' condition used along the side faces enforced a reflection of the velocities near the boundary so that if the velocity vectors suggest flow out across the boundary, this outward flow is matched by a symmetrical inward flow. This gave no net flow across the side boundaries, but the velocities were not zero along (parallel to) the boundary

3.3. Empirical validation

Following Narsilio et al. (2009), the hydraulic conductivity values (k_{CFD}) listed on Table 3 were calculated using the applied hydraulic gradient and the velocity component in the flow (Z) direction, averaged across a perpendicular slice (grey dashed line in Fig. 8). These average velocities represent the discharge velocity (flow rate per unit area).

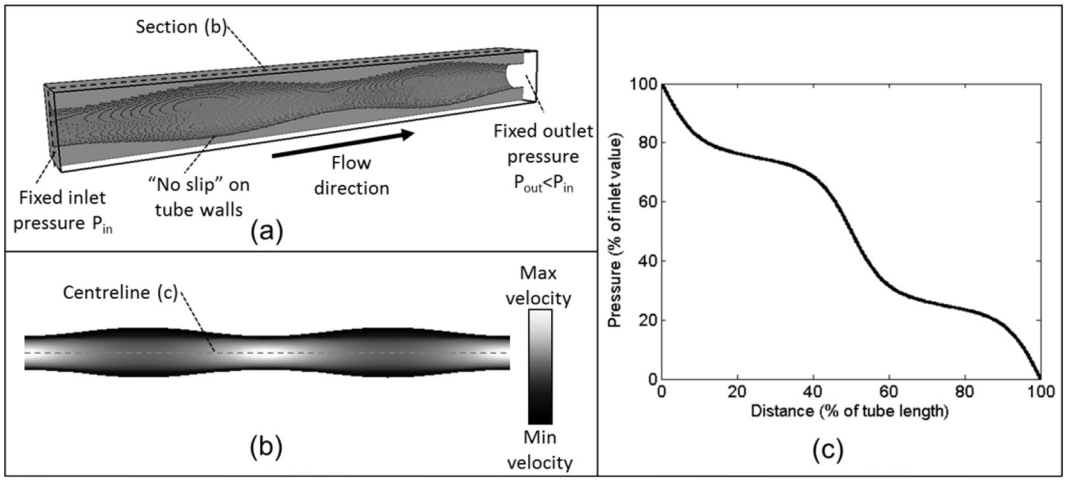

Fig. 5. Periodically constricted tube validation: (a) 3D image of voxelized tube, (b) velocity values, normalized between min and max values, on central 2D slice, and (c) pressure profile along center of tube.

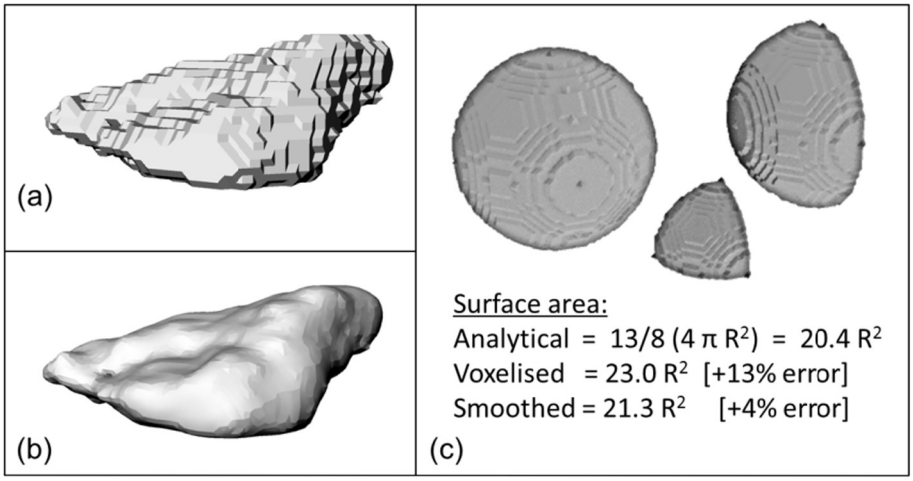

Fig. 6. Particle surface meshes: (a) from voxelized image, (b) after smoothing, and (c) voxelized sphere validation.

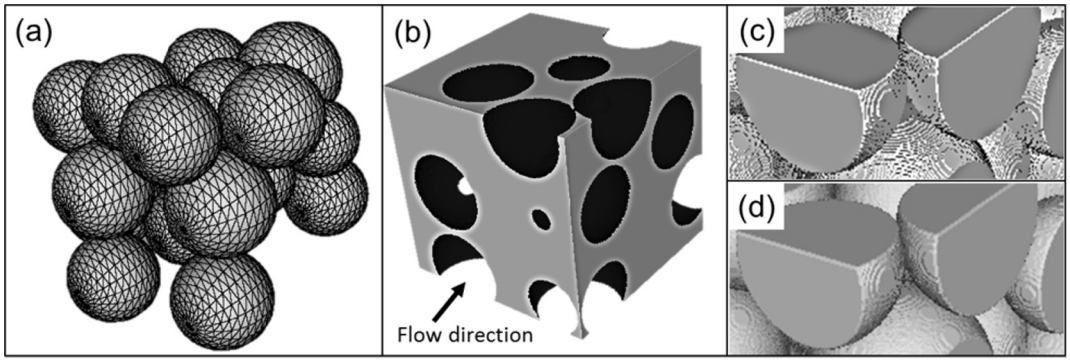

Fig. 7. Sensitivity analysis for voxel smoothing: (a) spheres generated in HelyxOS, (b) OpenFoam void mesh, (c) blow up of voxelized spheres before smoothing, and (d) after smoothing.

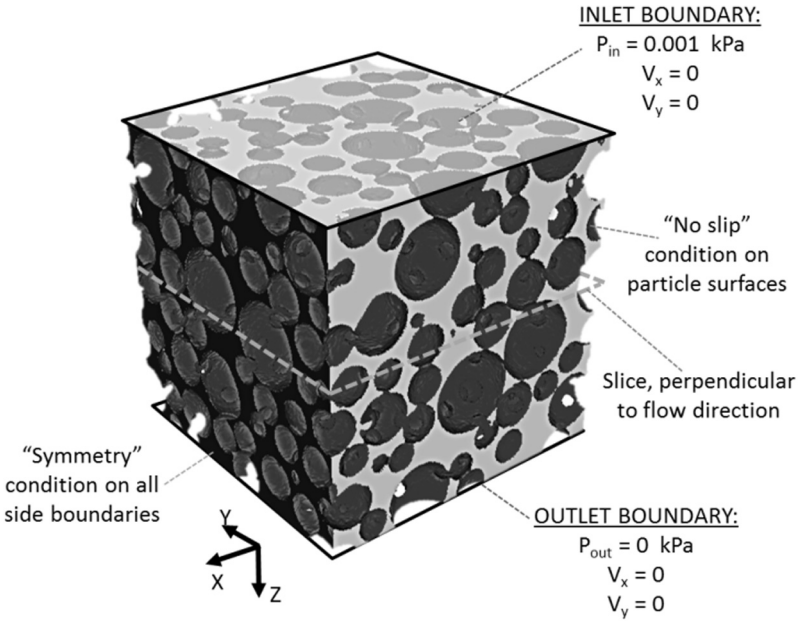

Fig. 8. 3D image of Beads-Cu3 sub-volume, showing CFD boundary conditions for vertical flow.

Table 3
Information measured from CFD simulations to estimate Kozeny-Carman constant.

Material	e	k_{CFD} (cm/s)	D_{10} (mm)	C_H (cm^{-1} s^{-1})	$S{\cdot}G_s$ (m^2/kg)	$S{\cdot}G_s$ estimate[a] (m^2/kg)	T	C_{KC}	k_0	$k_{Indraratna}$ (cm/s)
Sand-Cu3[1]	0.54	0.25	0.42	142	8.3	8.7	1.34	0.17	3.2	0.11
Sand-Cu3[2]	0.56	0.21	0.39	138	8.6	8.7	1.31	0.14	4.1	0.11
Sand-Cu1.5	0.60	0.24	0.44	124	9.9	9.9	1.28	0.18	3.4	0.13
Beads-Cu3	0.46	0.20	0.42	113	8.3	8.7	1.28	0.21	2.9	0.12
Beads-Cu1.5	0.60	0.29	0.48	126	9.8	9.9	1.24	0.21	3.1	0.12

[a] Using method proposed by Chapuis and Aubertin (2003).

Mass conservation was confirmed as the average velocity values agreed within ±1% considering all the slices in the image. Laboratory permeameter tests were carried out to measure the hydraulic conductivity values (k_{LAB}) for the four materials using samples produced from the same source material and applying the same preparation techniques. The tests followed the standard procedure (Head, 2011), using a constant head permeameter, 75 mm in diameter, as shown schematically in Fig. 2(b) and discussed in Dai (2014). Samples were constructed with a range of densities by varying the number of taps applied to the side of the cell with a nylon headed hammer. The samples were then wetted slowly from the base. Full saturation of the samples may not have been achieved using this approach and a subset of additional tests performed, where the samples were de-aired by applying a vacuum, found no significant effect on the hydraulic conductivity (<2% difference). Fig. 9 shows that four out of the five CFD results give k_{CFD} values which compare favorably with the laboratory data.

The k_{CFD} values were also compared with the commonly used Hazen (1892) empirical formula for cohesionless material, $k = C_H D_{10}^2$, where C_H is an empirically derived constant. The C_H values recommended in the literature are typically between 100 and 150, where k and D_{10} have units of cm/s and cm (Carrier, 2003). The Hazen formula is crude; however, it is reassuring that the CFD results lie within the range of k values predicted using this equation. The C_H values back calculated from the CFD results are listed in Table 3 and show no observable pattern with C_u or particle shape, confirming Carrier's (2003) observation that C_H does not have a useful physical significance.

The CFD result for Sand-Cu3[1] is approximately 25% higher than the laboratory range. As noted above, the increased void ratio in Sand-Cu3[1] should result in a higher hydraulic conductivity, but there will always be some discrepancy between permeameter results and measurements in a small sub-volume, due to physical boundary effects such as increased void ratio near the cell wall (Marketos and Bolton, 2010) and incomplete saturation (Head, 2011). The results are all within the range of uncertainty of typical predictive methods; hence, the CFD results are deemed to be plausible.

4. Observations of fluid flow

4.1. Flow velocity

Previous studies using CFD simulations of images of granular media (e.g., Narsilio et al., 2009; Zaretskiy et al., 2010) have highlighted the formation of preferential flow paths within the CFD models and that local velocities can vary significantly even within a single void constriction. Local pressure and velocity fields, on a representative 2D plane through the 3D simulation of Sand-Cu3[1], are pre-

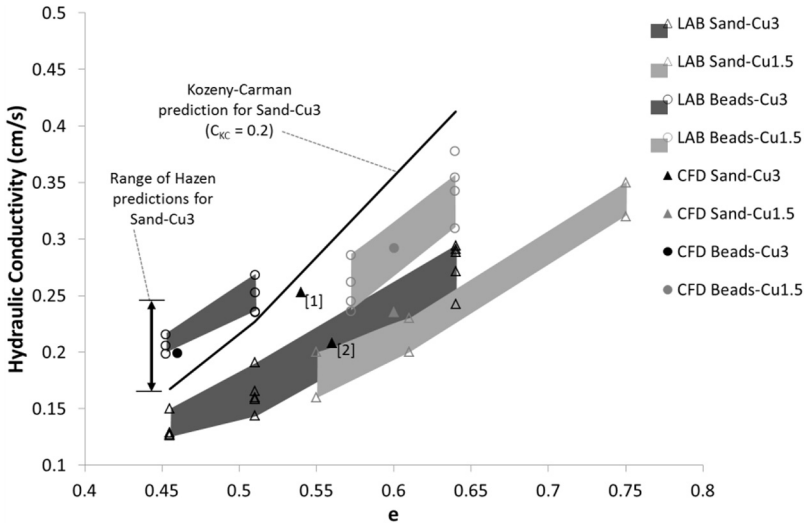

Fig. 9. Comparison of hydraulic conductivity from laboratory tests and CFD simulations.

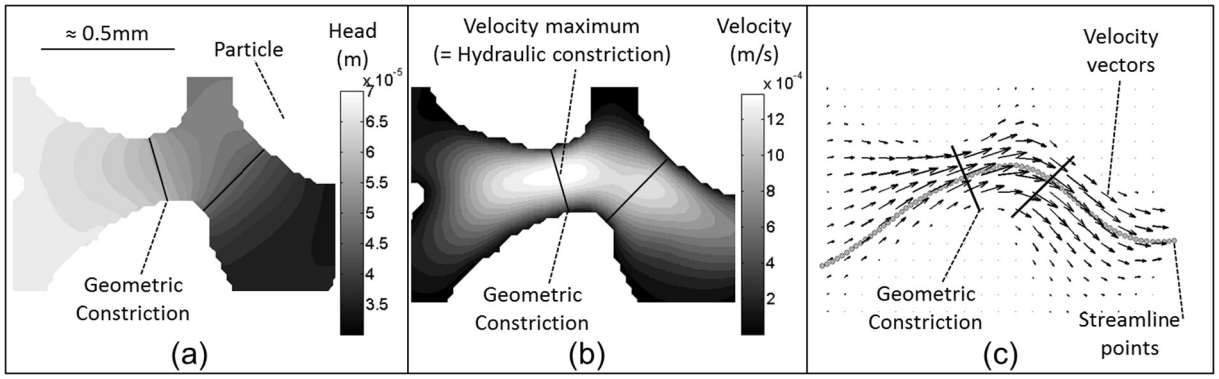

Fig. 10. CFD simulation results: (a) Head contours, (b) velocity contours, and (c) velocity vectors and streamline.

sented in Fig. 10. The head contours shown in Fig. 10(a) support the earlier hypothesis; contours are closer together in the vicinity of constrictions, indicating a steeper hydraulic gradient. Due to the conservation of mass, velocities increase significantly in the constrictions where the flow is forced through a narrower cross sectional area, producing the local maxima visible as the lighter shaded areas in Fig. 10(b). These local velocity maxima represent the locations where the fluid is most constrained; they were defined by Taylor et al. (2016) as 'hydraulic constrictions'.

The velocities shown in Fig. 10(b) are local velocity magnitudes, but the CFD results include velocity components in three Cartesian directions, producing the velocity vectors shown in Fig. 10(c). It is important to note that hydraulic constrictions (local velocity maxima, highlighted in Fig. 10(b)) occur close to the geometric constrictions, but do not necessarily occur at the center of the geometric constriction, nor is the flow orientation exactly perpendicular to the geometric constriction (Fig. 10(c)). It should be noted that 2D slices from 3D images can be misleading, but the difference in orientation between geometric constrictions and velocity maxima has been demonstrated in 3D by Taylor et al. (2016). Many text books (e.g., Harr, 1990; Cedergren, 1989) suggest that the actual velocity in voids can be approximated by the 'seepage velocity', $v_{seepage} = \frac{v_{discharge}}{n}$, where n is the porosity. Fig. 11(a) shows discharge and seepage velocities for Sand-Cu3[1], compared against the cumulative distribution of velocities from the CFD simulation (including both velocity magnitude and the component in the flow (Z) direction). Velocity magnitudes normalized by seepage velocity are shown in Fig. 11(b) for all five specimens. The seepage velocity crosses the CFD data very close to the median point. However, in all five materials, there are velocities 6–8 times larger than the seepage velocity at some locations within the void space. This has important implications in the study of erosion, as some mobile particles will experience velocities 6–8 times higher than the seepage velocity and the drag forces will be higher than those calculated based on the seepage velocity.

4.2. Head loss in constrictions

Streamlines have been used in a number of studies on porous rocks (e.g., Pereira Nunes et al., 2015; Zaretskiy et al., 2010) to identify the paths taken by fluid through the void space. Pereira Nunes et al. (2015) presented a

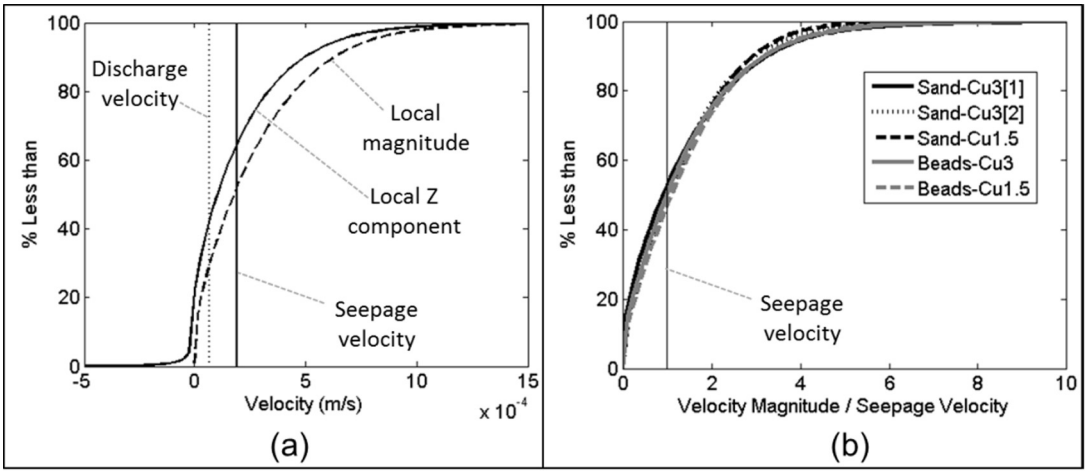

Fig. 11. Cumulative distributions of local velocities, (a) Sand-Cu3[1] and (b) all simulations, showing velocity magnitude normalized by seepage velocity.

simple method to generate streamlines from 3D velocity vector fields by selecting a start position; following the local velocity vector over a short distance to obtain a new position; then interpolating to find the new velocity vector at this position; and so on to produce a series of points along a streamline, as shown by the grey dots in Fig. 10(c). Streamlines are used here to measure the tortuosity, T (as described by Bayesteh and Mirghasemi (2015) and Guo (2015)), and to generate profiles of head loss as fluid flows through the void space. The cumulative distance, l, along each streamline is measured, as well as the shortest (straight line) distance from the beginning to the end of the streamline, s, and $T = l/s$. For each specimen, 1000 streamlines were generated, starting at a random location near the inflow boundary and continuing until they reached the outflow boundary. Geometric constrictions were defined as 3D planes using the watershed method and the points where streamlines crossed constriction planes were recorded. Fig. 12(a) shows head profiles along twenty streamlines, clearly demonstrating that the hydraulic gradient is not constant at the sub-grain-scale; rather, the head-position curve forms a stepped shape. Fig. 12(b) shows a single streamline with geometric constrictions marked as crosses, supporting the hypothesis that head losses are significantly larger in the constrictions than elsewhere in the void space.

To quantify the proportion of head loss occurring at constrictions, a rational approach was needed to differentiate the flow in the main voids from the flow in the constrictions. Thus, the head loss profiles were simplified to a series of linear segments (Fig. 12(c)). The hydraulic gradient was measured at each constriction, and the gradient at the midpoint between neighboring constrictions was then measured to give an indication of the hydraulic gradient in the larger parts of the voids. Finally, these gradients were extrapolated linearly and their intersections were found, forming the grey line in Fig. 12(c). While this linearized profile provides a very simple, efficient and repeatable method to partition head loss in constrictions from the head loss in voids, it systematically overestimates the head loss at constrictions, producing errors (denoted by ε in Fig. 12(d)); typically $\varepsilon/\Delta H_{cons} < 5\%$.

The streamlines used in the above analyses do not necessarily pass through the center of constrictions. To address this, and the subjectivity of defining constrictions, an alternative method was also used, based on hydraulic constrictions (local velocity maxima, Fig. 10(b)). In this method, streamlines started at the velocity maxima and were advanced forwards and backwards a short distance into the voids. The hydraulic gradient representing the larger voids was defined as the point of inflection in the head loss profile, as shown in Fig. 12(d). To explain this decision, the hydraulic gradient ($\Delta H/\Delta L$) is steepest at the constriction and it becomes less steep ($\Delta^2 H/\Delta L^2 > 0$) as the void space becomes wider. When the streamline passes the center of the void, it starts to move towards the next constriction; and so, the hydraulic gradient becomes steeper again ($\Delta^2 H/\Delta L^2 < 0$). Hence, the center of the void can be defined as the point of inflection, where the sign for $\Delta^2 H/\Delta L^2$ changes.

Tables 4 and 5 present the relative proportion of head loss in constrictions, quantified using the methods described in Fig. 12(c and d), as well as the approximate length of constrictions relative to the wider voids spaces. Table 4 also includes the spacing between constrictions, measured along streamlines and normalized by median particle size (D_{50}). In all specimens, whether full length or local stream lines are considered, approximately 65–75%

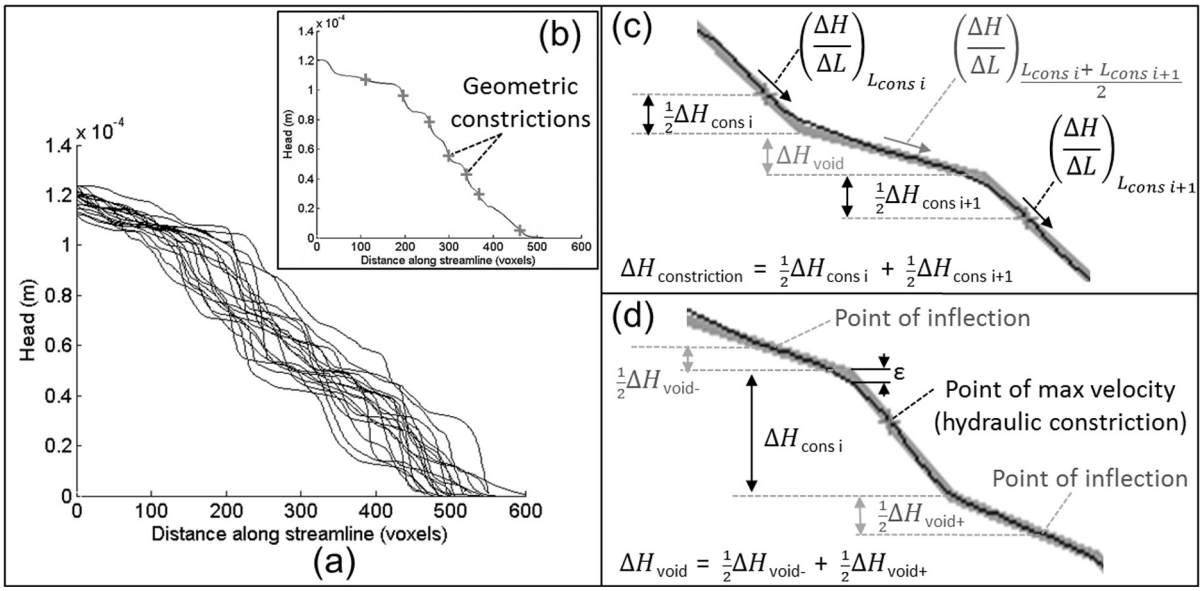

Fig. 12. Head loss in Sand-Cu3[1]: (a) results from 20 streamlines, (b) single streamline, (c) "geometric constriction" linearization, and (d) "hydraulic constriction" linearization.

Table 4
Summary of head loss and distance properties from full length streamlines.

Material	Proportion of head loss in constrictions	Proportion of length in constrictions	Constriction spacing/D_{50}
	Mean (Standard dev.)		
Sand-Cu3[1]	71% (12%)	38% (9%)	0.8 (0.4)
Sand-Cu3[2]	70% (11%)	38% (9%)	0.7 (0.3)
Sand-Cu1.5	64% (13%)	38% (11%)	1.2 (0.6)
Beads-Cu3	72% (11%)	39% (10%)	0.6 (0.3)
Beads-Cu1.5	69% (13%)	39% (10%)	0.9 (0.5)

Table 5
Summary of head loss and distance properties from local streamlines at hydraulic constrictions.

Material	Proportion of head loss in constrictions	Proportion of length in constrictions
	Mean (Standard dev.)	
Sand-Cu3[1]	77% (12%)	37% (8%)
Sand-Cu3[2]	77% (11%)	37% (8%)
Sand-Cu1.5	76% (12%)	37% (8%)
Beads-Cu3	77% (12%)	39% (8%)
Beads-Cu1.5	77% (11%)	39% (7%)

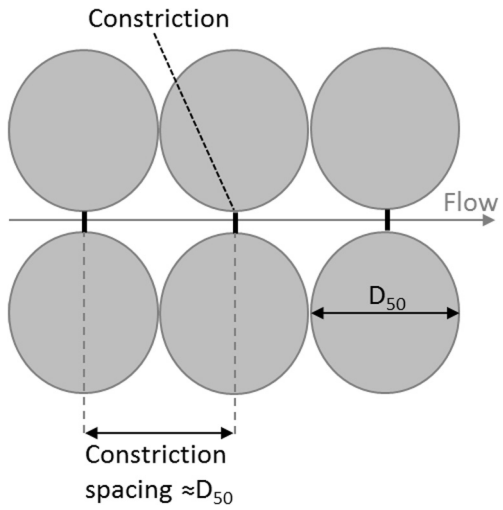

Fig. 13. Constriction spacing in 2D ideal packing of uniform spheres.

of the total head loss occurs in the constrictions, even though they account for less than 40% of the total length along streamlines. Analyses using hydraulic constrictions and short streamlines (Table 5) show similar results for all materials; however, streamlines running the full length of the simulation (Table 4) indicate some dependence on the type of material. Increasing the C_u value from 1.5 to 3 resulted in a noticeable increase (3–7%) in the proportion of head loss in constrictions, while changing from sand to glass beads resulted in a 1–5% increase. These increases in the proportion of head loss at constrictions are due to a combination of two factors: one is the increase in the number of small constrictions as C_u *increases*, as shown in Fig. 1, and the other, the more dominant one, appears to be the reduction in the spacing between constrictions when C_u increases and when there is a change in particle shape (sand to beads), as shown in Table 4. Fig. 9 shows a significant difference in the hydraulic conductivity between Sand-Cu3[1] and [2], even though they have very similar CSDs, suggesting that the difference is caused by a small difference in the constriction spacing (Table 4). The standard deviations are quite high for all the head loss and distance values, indicating that the behaviour for a particular constriction or streamline may vary significantly from the average for the whole material.

Analytical models have been used to estimate the spacing between constrictions; an example is shown in Fig. 13, with a constriction spacing equal to D_{50}. Wu et al. (2012) proposed alternative analytical methods, suggesting constriction spacings of less than half of D_{50}. The results in Table 4 suggest that while relatively uniform materials can have constriction spacing close to D_{50}, the spacing decreases for higher C_u values and also for spherical particles relative to sands. None of the measured values were as low as those suggested by Wu et al. (2012); however, Wu et al. try to estimate the spacing between soil layers, rather than the distance between constrictions accounting for the tortuosity of the flow.

For the flow in a pipe, the head loss due to a constriction has long been recognized as the 'Venturi effect' and the magnitude of the head loss is related to the relative size of the constriction as $v_{constric}^2 - v_{pipe}^2 = 2g\Delta H$ (Douglas et al., 1995), where ΔH is the head loss between the pipe and the constriction, $v_{constric}$ and v_{pipe} are the mean velocities across the constriction and the pipe, respectively, while $A_{constric}$ and A_{pipe} are the corresponding cross sectional areas. However, $v_{constric} \cdot A_{constric} = v_{pipe} \cdot A_{pipe}$ giving

$$\frac{2g\Delta H}{v_{constric}^2} = 1 - \frac{A_{constric}^2}{A_{pipe}^2} \quad (1)$$

For constrictions in sands, it is expected that smaller constrictions will produce larger head losses, but the quantitative relationship in Eq. (1) cannot easily be applied, both because the geometry of the entry and exit to the constrictions is highly irregular and the fluid crossing the wider parts of the voids will divide amongst a large number of constrictions; hence $v_{constric} \cdot A_{constric} \neq v_{precedingvoid} \cdot A_{precedingvoid}$.

Relating the head loss at a constriction to its size is challenging, because local heterogeneity in the flow can result in two constrictions with the same size, but different orientations, experiencing very different velocities, and hence,

very different head losses. To account for this heterogeneity, Fig. 14(a) shows head loss values at each hydraulic constriction in the Sand-Cu3[1] material, normalized by the average velocity across that constriction; the data are plotted against (constriction diameter)$^{-1}$ as this produces a clearer trend with head loss. The constriction diameter is the diameter of the largest sphere which can pass through the constriction. While there is significant scatter in the data in Fig. 14(a), smaller constrictions produce a greater head loss per unit velocity than large constrictions, which agrees with the results of Yazdchi and Luding (2013) and Indraratna et al. (2012) for flow and constriction properties averaged over larger volumes. In Fig. 14(a), a linear fit, based on the mean ratio of head/velocity (constriction diameter)$^{-1}$, produces a relatively poor r^2 value of 0.5. However, quadratic and cubic spline regressions were also attempted; this produced r^2 values of only 0.52 and 0.53, respectively. As an alternative, the head losses are plotted in Fig. 14(b) based on the left and right sides of Eq. (1), where the cross sectional areas were approximated by the square of the distance map values (i.e., the radius of the void space) at the constrictions and at the largest point in the preceding voids. Smaller constrictions (where $1-A^2_{constric}/A^2_{void}$ tends to 1) produce much higher head losses but, as noted earlier, there is not a clear trend due to the complexity of the void geometry and there is definitely not a linear relationship, as suggested by Eq. (1), for the flow in pipes.

Despite the low r^2 values, linear fits for all five materials are presented in Fig. 14(c), in terms of the mean and ±1 standard deviation, and enable a general overview of the data for all the samples. While results for the glass bead samples are similar, the angular sand particles produce higher head losses per unit velocity, with the highest head losses in the more uniform Sand-Cu1.5 sample. The specific surface values, S, were higher for angular particles than for spheres (shown in Table 3 in terms of $S{\cdot}G_s$ rather than S, to eliminate the effect of differing G_s between sands and glass beads). However, these differences were small compared to the difference in hydraulic conductivity (Fig. 9). These results indicate that, while the head loss is largely controlled by the size of the constrictions, the shape of the constrictions (governed by the angularity of the particles) also has an impact on the hydraulic conductivity.

5. Evaluation of existing models

5.1. Kozeny-Carman

The Kozeny-Carmen equation (Carman, 1937) was originally developed to estimate specific surface, S, for industrial powders with known hydraulic conductivity, because S could not be measured directly (Chapuis and Aubertin, 2003). The equation considers a group of capillary tubes to be an appropriate analogue to the connected void space in a soil. The velocity : head loss relationship for a single tube is given by Poiseuille's law, $v=\frac{\rho_w R^2}{8\mu_w}i$, where v is the average velocity, ρ_w is the fluid density, R is the tube radius, μ_w is the dynamic viscosity of the fluid and i is the hydraulic gradient. The Kozeny-Carman equation is derived by using the geometric properties of the soil to determine a value for R to represent the void space. A version of the Kozeny-Carman equation, described by Mitchell and Soga (2005), is given as

$$k=\left[\frac{1}{k_0}\right]\frac{\gamma_w}{\mu_w}\frac{e^3}{T^2S_0^2(1+e)}=\left[\frac{1}{k_0T^2}\right]\frac{g}{\mu_w\rho_w}\frac{e^3}{S^2G_s^2(1+e)} \quad (2)$$

where k_0 is an empirical constant, γ_w is the unit weight of the fluid, S_0 is the surface area per unit volume, and G_s is the specific gravity of the soil. This equation appears to capture the relationship between k and the void ratio, as well as particle size and gradation (linked to S). Some authors have suggested that it is valid for estimating hydraulic conductivity in sands, but not in clays (Carrier, 2003; Chapuis and Aubertin, 2003; Lambe and Whitman, 1969). However, this then requires values for S, T, and k_0 which cannot be measured. Chapuis and Aubertin (2003) present a simple analytical method to estimate S based on the PSD, which assumes spherical particles. Referring to Table 3, $S{\cdot}G_s$ values estimated using the method by Chapuis and Aubertin (2003) are within ±5% of the values

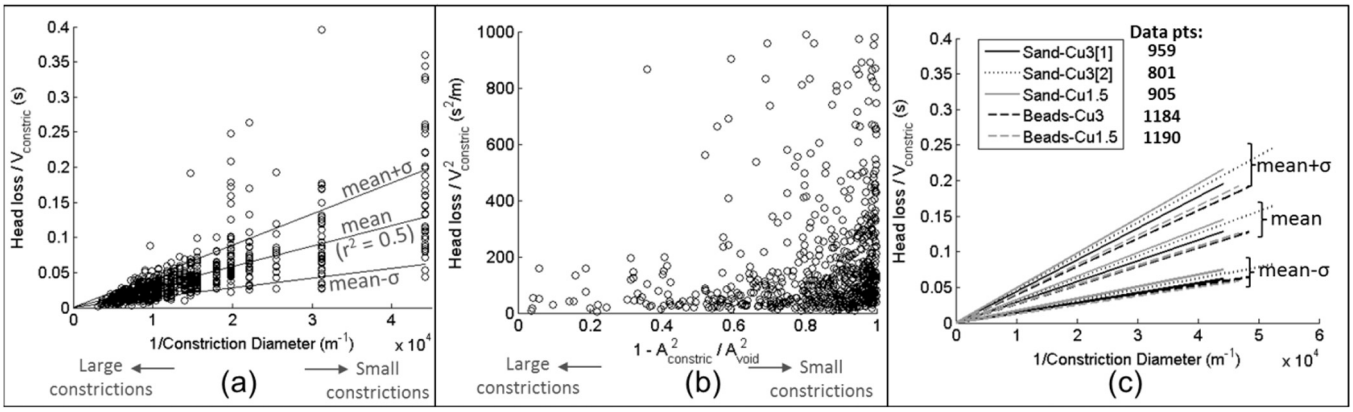

Fig. 14. Head loss in individual constrictions: (a) Head loss (normalized by velocity) vs 1/constriction size for Sand-Cu3[1] and (b) for all materials, and (c) normalized head loss vs area ratio.

measured from the microCT generated data. Guo (2015) presents upper and lower bound estimates of T for various porous media, with values of approximately 1.2–1.7 for the porosity range discussed here, while Mitchell and Soga (2005) suggest T values of $\sqrt{2}$. Referring to Table 3, these estimates for T are not unreasonable.

Mitchell and Soga (2005) suggest $k_0 = 2.5$ and Chapuis and Aubertin (2003) suggest combining k_0 and T into an empirical parameter C_{KC}, giving

$$k = C_{KC} \frac{g}{\mu_w \rho_w} \frac{e^3}{S^2 G_s^2 (1+e)} \tag{3}$$

Back-calculated C_{KC} values are also shown in Table 3; values for the sands are lower than the suggested values of 0.2 (Carrier, 2003; Chapuis and Aubertin, 2003), while 0.2 appears to be a good estimate for the two beads specimens, although there are significant differences between beads and sands. This is evidence that, while the Kozeny-Carman equation can account for particle size, gradation, and void ratio, it does not account for particle shape. Back-calculated k_0 values are higher than the value of 2.5 suggested by Mitchell and Soga (2005) and there is no clear pattern with C_u or particle shape. As such, it appears that accounting for tortuosity does not improve the accuracy of the Kozeny-Carman equation. These results suggest that if hydraulic conductivity data are available for a particular sand, it may be possible to use the Kozeny-Carman equation to account for small changes in PSD or the void ratio, but selecting appropriate C_{KC} or k_0 values in the absence of laboratory permeameter data will be extremely challenging.

5.2. Indraratna et al. (2012)

Indraratna et al. (2012) estimated constriction sizes analytically for spherical particles in ideal configurations. They compared these CSD estimates with permeameter data for 60 samples of sands and gravels and proposed the following empirical correlation:

$$k_{Indraratna} = 36.91 (D_c^m)^{1.644} \tag{4}$$

D_c^m is the mean constriction diameter and values were determined from the CSDs shown in Fig. 1. Eq. (4) was used to calculate the hydraulic conductivity estimates, $k_{Indraratna}$, given in Table 3. These estimates differ from the CFD results and lab tests by a factor of approximately 2. Given that Eq. (4) was based on a large dataset of materials similar to those examined here, the most likely explanation for this discrepancy is the difference between the CSD measured from images of real specimens and the approximate values used by Indraratna et al. (2012).

6. Conclusions

This paper has presented the results of CFD simulations on microCT images of sands and glass beads. The CFD results were validated against permeameter data, as well as analytical solutions, and were found to agree well provided that the voxelized images were smoothed before generating the CFD meshes. 3D datasets of pressures and velocities at the sub-grain-scale were analyzed to determine local velocities and head losses, as well as fluid streamlines, tortuosity, and specific surface values, none of which can be accurately measured in the laboratory.

The CFD results show that local velocities at the sub-grain-scale vary significantly from volume-averaged velocities (discharge or seepage velocity), with velocities 6–8 times larger than the seepage velocity occurring locally within the void space. This should be taken into account when modelling hydro-mechanical processes including seepage, erosion, and contaminant transport. As imaging hardware develops, it will be possible to carry out similar studies on a wider range of C_u values but, for the range studied here, the seepage velocity gives a reasonable estimate of the median velocity.

The hypothesis that hydraulic conductivity is governed by void constrictions has been suggested by previous numerical (Yazdchi and Luding, 2013) and empirical (Indraratna et al., 2012) models, but the results presented in the current paper provide a new approach for visualizing and quantifying the proportion of head loss which occurs in the constrictions. The main conclusions are:

- Approximately 65–75% of the total head loss occurs at the constrictions, even though the constrictions account for <40% of the total length travelled through the void space.
- An increase in C_u or a change from sand to spherical particles increases the proportion of head loss at the constrictions. This appears to be dominated by the spacing between the constrictions, rather than the changes in the constriction size distribution.
- Five samples (four materials + 1 repeat) with varying particle sizes, gradations, void ratios, and particle shapes, produce similar relationships between head loss per unit velocity and constriction size.
- While the constriction size governs head loss, the shape of the constrictions (governed by the angularity of the particles) has an impact, with larger head losses in angular materials. The irregular shapes of constrictions produce much higher head losses than those predicted by the Venturi effect for pipes.
- The spacing between constrictions is close to D_{50} for sand with $C_u = 1.5$, but this spacing decreases for higher C_u and for spherical particles.
- Descriptions of void geometry (especially constrictions) are highly subjective, and thus, alternative definitions are considered in this study. The results vary between methods, highlighting that geotechnical engineers using models based on void geometry must consider alternative definitions and determine which is the most appropriate for their model.

The data are used to evaluate previously proposed expressions for hydraulic conductivity, which were developed using grain-scale models. The back calculation of constants from the Kozeny-Carman equation produces values which differ from those in the literature by roughly 30–60%. While the Kozeny-Carman equation accounts for particle size, gradation, and void ratio, it does not account for changes in particle shape. The empirical relationship between constriction size and hydraulic conductivity proposed by Indraratna et al. (2012) does not agree with the CFD data.

Acknowledgements

The authors would like to thank Lucy Diggens and the whole team at the Centre for Micromorphology, Queen Mary University of London, for their expertise in microCT scanning, as well as Alan Bolsher, Graham Keefe and Steve Ackerley at the Imperial College soils laboratory for their inexhaustible wisdom and resourcefulness. This work was undertaken as part of PhD research funded by the Engineering and Physical Sciences Research Council under a Doctoral Training Grant scholarship.

References

Altuhafi, F., O'Sullivan, C., Cavarretta, I., 2013. Analysis of an image based method to quantify the size and shape of sand particles. J. Geotech. Geoenviron. Eng. 139 (8), 1290–1307.

Bayesteh, H., Mirghasemi, A.A., 2015. Numerical simulation of porosity and tortuosity effect on the permeability in clay: microstructural approach. Soils Found. 55, 1158–1170.

Carman, P.C., 1937. Fluid flow through granular beds. Trans. Inst. Chem. Eng. Lond. 15, 150–166.

Carrier, P.C., 2003. Goodbye, Hazen; Hello, Kozeny-Carman. J. Geotech. Geoenviron. Eng. ASCE 129 (11), 1054–1056.

Cashman, P.M., Preene, M., 2001. Groundwater Lowering in Construction: A Practical Guide, first ed. Spon, London.

Cavarretta, I., O'Sullivan, C., Ibraim, E., Lings, M., Hamlin, S., Wood, D.M., 2012. Characterization of artificial spherical particles for DEM validation studies. Particuology 10, 209–220.

Cedergren, H.R., 1989. Seepage, Drainage and Flow Nets, third ed. Wiley, New York.

Chapuis, R.P., Aubertin, M., 2003. Predicting the coefficient of permeability of soils using the Kozeny-Carman equation. EPM-RT-2003-03.

Chareyre, B., Cortis, A., Catalano, E., Barthelemy, E., 2012. Pore-scale modeling of viscous flow and induced forces in dense sphere packings. Transp. Porous Media 94, 595–615.

Cnudde, V., Boone, M.N., 2013. High-resolution X-ray computed tomography in geosciences: a review of the current technology and applications. Earth-Sci. Rev. 123, 1–17.

Dai, Q., 2014. Permeameter Tests to Relate Particle Size Distribution to the Permeability and Stability of Selected Granular Filters. Imperial College London.

Dallo, Y.A.H., Wang, Y., 2016. Determination of controlling constriction size from capillary tube model for internal stability assessment of granular soils. Soils Found. 56, 315–320.

Dong, H., Blunt, M.J., 2009. Pore-network extraction from micro-computerized-tomography images. Phys. Rev. E 80, 036307-1–036307-11.

Douglas, J.F., Gasiorek, J.M., Swaffield, J.A., 1995. Fluid Mechanics, third ed. Longman Scientific & Technical, Harlow.

Engys, 2015. Helyx-OS.

Fetter, C.W., 1994. Applied Hydrogeology, third ed. Prentice Hall, New Jersey.

Fitts, C.R., 2012. Groundwater Science, second ed. Academic Press (Elsevier), Waltham, MA.

Fonseca, J., O'Sullivan, C., Coop, M.R., Lee, P.D., 2012. Non-invasive characterisation of particle morphology of natural sands. Soils Found. 52 (4), 712–722.

Fonseca, J., Sim, W.W., Shire, T., O'Sullivan, C., 2013. Micro-structural analysis of sands with varying degrees of internal stability. Geotechnique 64, 405–411.

Galindo-Torres, S.A., 2013. A coupled discrete element lattice Boltzmann method for the simulation of fluid-solid interaction with particles of general shapes. Comput. Methods Appl. Mech. Eng. 265, 107–119.

Guo, P., 2015. Lower and upper bounds for hydraulic tortuosity of porous materials. Transp. Porous Media 109, 659–671.

Harr, M.E., 1990. Groundwater and Seepage. Dover Publications, New York.

Hazen, A., 1892. Some physical properties of sands and gravels, with special reference to their use in filtration. In: Massachusetts State Board of Health, 24th Annual Report, Pub No. 34.

Head, K.H., 2011. Manaul of Soil Laboratory Testing – Vol. 2: Permeability, Shear Strength and Compressibility Tests, third ed. Wiley, New York.

Homberg, U., Baum, D., Wiebel, A., Prohaska, S., Hege, H.-C., 2014. Definition, extraction, and validation of pore structures in porous materials. In: Bremer, P.-T., Hotz, I., Pascucci, V., Peikert, R. (Eds.), Topological Methods in Data Analysis and Visualization III. Springer, pp. 235–248.

Indraratna, B., Nguyen, V.T., Rujikiatkamjorn, C., 2012. Hydraulic conductivity of saturated granular soils determined using a constriction-based technique. Can. Geotech. J. 49, 607–613.

Ishihara, K., 1993. Liquefaction and flow failure during earthquakes. Géotechnique 43, 351–451.

Kenney, T.C., Chahal, R., Chiu, E., Ofoegbu, G.I., Omange, G.N., Ume, C.A., 1985. Controlling constriction sizes of granular filters. Can. Geotech. J. 22, 32–43.

Kézdi, A., 1979. Soil Phys.: Sel. Top.

Kim, Y.S., Whittle, A.J., 2009. Particle network model for simulating the filtration of a microfine cement grout in sand. J. Geotech. Geoenviron. Eng. ASCE 135, 224–236.

Lambe, T.W., Whitman, R.V., 1969. Soil Mechanics. Wiley, New York.

Lindquist, W.B., Venkatarangan, A., Dunsmuir, J., Wong, T.F., 2000. Pore and throat size distributions measured from synchrotron X-ray tomographic images of Fontainebleu sandstones. J. Geophys. Res. 105, 21509–21527.

Marketos, G., Bolton, M.D., 2010. Flat boundaries and their effects on sand testing. Int. J. Numer. Anal. Meth. Geomech. 34, 821–837.

Mitchell, J.K., Soga, K., 2005. Fundamentals of Soil Behaviour, third ed. Wiley, New Jersey.

Mostaghimi, P., Blunt, M.J., Bijeljic, B., 2013. Computations of absolute permeability on micro-CT images. Math. Geosci. 45, 103–125.

Narsilio, G.a., Buzzi, O., Fityus, S., Yun, T.S., Smith, D.W., 2009. Upscaling of Navier-Stokes equations in porous media: theoretical, numerical and experimental approach. Comput. Geotech. 36, 1200–1206.

OpenFOAM Foundation, 2014. OpenFOAMwiki [WWW Document]. URL: <https://openfoamwiki.net/index.php/OpenFOAM_guide/The_SIMPLE_algorithm_in_OpenFOAM> (accessed 11.9.15).

OpenFOAM Foundation, 2015. OpenFOAM 2.4.0.

Otsu, N., 1979. A threshold selection method from gray-level histograms. IEEE Trans. Syst. Man Cybern. 9, 62–66.

Pereira Nunes, J.P., Bijeljic, B., Blunt, M.J., 2015. Time-of-flight distributions and breakthrough curves in heterogeneous porous media using a pore-scale streamline tracing algorithm. Transp. Porous Media 109, 317–336.

Piller, M., Casagrande, D., Schena, G., Santini, M., 2014. Pore-scale simulation of laminar flow through porous media. J. Phys: Conf. Ser. 501, 1–13.

Raeini, A.Q., Blunt, M.J., Bijeljic, B., 2012. Modelling two-phase flow in porous media at the pore scale using the volume-of-fluid method. J. Comput. Phys. 231, 5653–5668.

Rajon, D.A., Patton, P.W., Shah, a.P., Watchman, C.J., Bolch, W.E., 2002. Surface area overestimation within three-dimensional digital images and its consequence for skeletal dosimetry. Med. Phys. 29, 682–693.

Rasband, W.S., 2012. ImageJ [WWW Document]. U.S. Natl. Institutes Heal. Bethesda, Maryland, USA, 1997–2012. URL: <http://imagej.nih.gov/ij/> (accessed 11.27.13).

Reboul, N., Vincens, E., Cambou, B., 2010. A computational procedure to assess the distribution of constriction sizes for an assembly of spheres. Comput. Geotech. 37, 195–206.

Robert McNeel & Associates, 2015. Rhinoceros 3D.

Shire, T., O'Sullivan, C., 2016. Constriction size distributions of granular filters: a numerical study. Geotechnique 66 (10), 826–839.

Sisavath, S., Jing, X., Zimmerman, R.W., 2001. Creeping flow through a pipe of varying radius. Phys. Fluids 13, 2762.

Taylor, H.F., O'Sullivan, C., Sim, W.W., 2015. A new method to identify void constrictions in micro-CT images of sand. Comput. Geotech. 69, 279–290.

Taylor, H.F., O'Sullivan, C., Sim, W.W., 2016. Geometric and hydraulic void constrictions in granular media. J. Geotech. Geoenviron. Eng. ASCE 142 (11).

Wu, L., Nzouapet, B.N., Vincens, E., Bernat-Minana, S., 2012. Laboratory experiments for the determination of the constriction size distribution of granular filters. Int. Conf. Scour Eros., 233–240

Yazdchi, K., Luding, S., 2013. Upscaling and microstructural analysis of the flow-structure relation perpendicular to random, parallel fiber arrays. Chem. Eng. Sci. 98, 173–185.

Zaretskiy, Y., Geiger, S., Sorbie, K., Forster, M., 2010. Efficient flow and transport simulations in reconstructed 3D pore geometries. Adv. Water Resour. 33, 1508–1516.

Zeghal, M., El Shamy, U., 2004. A continuum-discrete hydromechanical analysis of granular deposit liquefaction. Int. J. Numer. Anal. Methods Geomech. 28, 1361–1383.